RSC Advances

ROYAL SOCIETY OF CHEMISTRY

PAPER

View Article Online
View Journal | View Issue

Cite this: *RSC Adv.*, 2021, **11**, 856

Bifunctional investigation of ultra-small SnO_2 nanoparticle decorated rGO for ozone sensing and supercapacitor applications

J. Jayachandiran,[a] J. Yesuraj,[b] M. Arivanandhan,[c] B. Muthuraaman,[b] R. Jayavel[c] and D. Nedumaran*[a]

Ultrasmall SnO_2 nanoparticles with an average size of 7 nm were synthesized by a hydrothermal method and composited with reduced graphene oxide (rGO) through an ultrasonic assisted solution process. The structural, functional, morphological and compositional properties of synthesised SnO_2 and rGO/SnO_2 were studied by XRD, FTIR, HRSEM, HRTEM, XPS and Raman analyses. The prepared materials were developed as a film over a PVA/KOH conductive layer coated substrate with varying thickness of 3, 5 and 7 μm to study their ozone sensing characteristics at room temperature. The physico-chemical properties reveal that the fabricated SnO_2 and rGO/SnO_2 nanocomposite films have a strong interaction with the ozone gas. Among the fabricated composite films rGO/SnO_2-S1 film exhibits high ozone sensing response (38%) at room temperature. Additionally, the electrochemical performance of SnO_2 and rGO/SnO_2 nanocomposites was analysed and the rGO/SnO_2 nanocomposite exhibited higher specific capacitance (545 F g^{-1}) than that of pure SnO_2 (236 F g^{-1}) at a current density of 1 A g^{-1} with higher cyclic stability (96%) than that of pure SnO_2 (86%) at the current density of 20 A g^{-1} for a continuous 5000 charge–discharge cycles. Thus, the rGO/SnO_2 nanocomposite showed an excellent ozone sensing and energy storage performance.

Received 1st December 2020
Accepted 16th December 2020

DOI: 10.1039/d0ra10137k

rsc.li/rsc-advances

Introduction

Globally, the energy demand and environmental pollution are two major challenges for the present and future generations. Rapidly increasing usage of automobiles and chemical industries produces toxic gases and hydrocarbons, which react with the atmospheric chemical species thus creating harmful diseases for humans and other living things. Ozone is one of the toxic and strong oxidizing gases, with wide usage in various industrial and medical fields.[1–5] It can be produced naturally in the upper level of the atmosphere, called outdoor ozone, and the ground level ozone can be produced by electrical discharge, household materials, *etc.* This could create acute health effects like pulmonary, cardiovascular and chronic diseases[6] when exceeding the limited threshold value of (0.08 ppm).[7] Moreover, ozone gas can be used in water purification, food processing, textile and ozone therapy for cancer treatment. Therefore, due to its widespread applications and toxicity, ozone sensing devices are highly essential for monitoring the ozone concentration.

An electric power-based device can be effectively used to overcome the addressed environmental issues like air pollution and generation of toxic molecules. In this process the performance of a device depends on the charge storage capacity of the energy storage devices like supercapacitors. But these devices may suffer from low energy density due to their limited storage capacity hence, it holds great demand to achieve long-life span with superior charge storage performance. The electrode material plays a vital role for the improvement of specific capacitance of the supercapacitor. These electrode materials store the energy based on different charge storage mechanism such as electric double layer capacitance (EDLC) and pseudocapacitance. The charge balance between the electrode and electrolyte produces the EDLC behaviour and the faradic charge transfer between the electrode and electrolyte through oxidation–reduction reaction, which is responsible for the pseudocapacitance behaviour. The electrochemical property of the electrode material can be enhanced by controlling the morphology,[8] particle size[9] and hybridisation of different types.[10–12] Hence, development of hybrid nanocomposite material with high power density and life cycle stability is essential to provide a favourable solution for sustainable usage. Meanwhile, numerous efforts have been exerted on the synthesis of novel metal oxide nanocomposites with required shape and

---

[a] *Central Instrumentation and Service Laboratory, University of Madras, Guindy Campus, Chennai 600 025, TN, India. E-mail: dnmaran@gmail.com; dnmaran@unom.ac.in*

[b] *Department of Energy, University of Madras, Guindy Campus, Chennai 600 025, TN, India*

[c] *Centre for Nanoscience and Technology, Anna University, Guindy, Chennai 600 025, TN, India*

structures for improving the sensing and energy storage performance of the device.

Transition metal oxides possess broad structural and morphological variations owing to their capability to form phases of different metal to oxygen ratios showing multiple stable oxidation states of the metal ions. Among them, SnO_2 has attracted cognizable interest owing to its strong chemical stability and out-standing optical and electrical features. It has been extensively used for gas sensing[13–16] and energy storage applications.[9] The chemical and physical features of tin oxide nano-crystalline material can be tuned by preparation methods that leads to the controlled surface morphology as well as grain size. Therefore, the preparation of SnO_2 nanoparticles with desired structure and morphology provides attractive physical and chemical features, which enables enhanced performance in gas sensing[17,18] and energy storage applications.[9] Though SnO_2 nanoparticles have a good interaction with ozone gas, its semiconducting nature and operating temperature restrict the sensing response. The problem associated with ozone sensing was resolved by coating Au or Ag conductive layer, before the deposition of the sensing material on the substrate.[19,20] This type of fabrication process increases the material cost as well as the complicated instrumentation for thin film deposition. Therefore, it is very essential to develop ways for controlling the structure, dimensions, interface and surface characteristics. In addition, hybridisation of graphene-based materials into SnO_2 nanoparticles is a wise-approach to enhance the surface area and conductivity of the sensing SnO_2 film with more active sites.[21–23] Further, the synergistic effect between graphene and metal oxides favours high transportation of electrolyte ions in the electrode material that leads to superior electrochemical performance than the pure metal oxides.[24–29]

In the present work, new approach has been adopted for the synthesis of ultra-small SnO_2 nanoparticles and the average size of the synthesised SnO_2 nanoparticles was achieved below 10 nm. The size reduced fine particles enables large surface area with more active sites, which in-turn enhanced the ozone sensing performance. The synthesised SnO_2 nanoparticles were composited with rGO nanosheets, which provide high sensitivity and high electrical conductivity during the exposure of ozone gas on the surface of the sensing film. The synthesised rGO/SnO_2 nanocomposite material showed improved ozone sensing response by morphological, optical and electrical variations than pure SnO_2 nanoparticles in the room temperature. Further, the composite materials exhibited higher specific capacitance value (545 F g^{-1}) at a current density of 1 A g^{-1} with higher cyclic stability of 96% at the current density of 20 A g^{-1} for continuous 5000 charge–discharge cycles.

Experimental

Chemicals

Pre-oxidized graphite flakes, Tin(II) chloride dihydrate ($SnCl_2\cdot 2H_2O$), diethylamine ($(CH_3CH_2)_2NH$), sodium nitrate ($NaNO_3$), potassium permanganate ($KMnO_4$), hydrochloric acid (HCl), sulfuric acid (H_2SO_4) and hydrogen peroxide (H_2O_2) were purchased from Sigma-Aldrich and used for the preparation of the nanocomposites. Ultra-pure water with resistivity of 18.2 MΩ cm^{-1} (Milli-Q Water, Millipore System) was used for all the preparation process.

Synthesis of tin oxide (SnO_2) nanoparticles

Tin(II) chloride dihydrate ($SnCl_2\cdot 2H_2O$) precursor material (1.327 g) was dissolved in ethanol solvent and stirred for 15 min. After that poly-vinyl alcohol (PVA) surfactant was added slowly and stirred for 30 min. Then, diethylamine ($(CH_3CH_2)_2NH$) was added as a precipitating agent, stirred for 15 min and transferred into the Teflon lined autoclave and maintained at 200 °C for 24 h. After cooling the autoclave to room temperature, the precipitate material was washed, filtered thrice and dried in a hot-air oven. Finally, the resultant material was grained in a mortar and stored in a vacuum desiccator for further studies.

Synthesis of rGO

Initially, the graphene oxide (GO) was synthesized from pre-oxidized graphite flakes by modified Hummer's method.[30,31] In an ice-bath, 1.5 g of $NaNO_3$, 115 mL of H_2SO_4 and 3 g of pre-oxidized graphite were mixed and stirred for 20 min. Then, 9 g of $KMnO_4$ was slowly added to the suspension under vigorous stirring condition and the temperature was maintained below 20 °C. After that, the temperature of the mixture was increased to 35 °C and continuously stirred for about 12 h. Then, 300 mL of DI water was added and heated to 98 °C. To minimize the residual manganese dioxide and permanganate, the suspension was diluted to 1 L using DI water and treated with 30 wt% of colorless H_2O_2. To neutralize the pH of the mixture, it was filtered and washed with DI water and 5 wt% of HCl aqueous solution. Subsequently, the product was dried at 40 °C under vacuum for about 24 h and the final form of GO was collected.[32] The prepared GO was reduced to rGO by adding thiourea as a reducing agent at 100 °C followed by continuous stirring for 24 h.

Preparation of rGO/SnO_2 nanocomposite

The rGO/SnO_2 nanocomposite material was prepared by the ultrasonic assisted solution process. Initially, 150 mL of rGO suspension was prepared by adding 0.125 g of rGO into the DI water and sonicated for 30 min. Then, 0.03125 g of SnO_2 nanoparticles were added to 50 mL of DI water and sonicated for 30 min. Both the solutions were mixed and sonicated for 45 min. After that the sample was collected by drying in a hot-air oven. Finally, the rGO/SnO_2 nanocomposite powder was obtained.

Fabrication of rGO/SnO_2 nanocomposite film

As reported in the previous work, the PVA/KOH conductive polymer coated sample exhibited very good response towards ozone gas sensing.[33] Therefore, the PVA/KOH conductive polymer was coated on the cleaned quartz substrate by dip-coating method. Then, the variable thickness of rGO/SnO_2 nanocomposite material was drop-casted layer by layer over the conductive layer and dried in a hot-air oven at 180 °C. The fabricated composite's sample thicknesses were measured and named as rGO/SnO_2-S1 (3 μm), rGO/SnO_2-S2 (5 μm) and rGO/SnO_2-S3 (7 μm), respectively.

Electrode preparation for electrochemical analysis

The electrochemical properties of prepared pure SnO_2 and rGO/SnO_2 nanocomposite were analysed by cyclic voltammetry (CV) with three electrode configurations using 1 M H_2SO_4 electrolyte at room temperature. The working electrode was fabricated by addition of 80 wt% of active material, 10 wt% acetylene black, and 10 wt% polyvinylidene fluoride (PVDF) binder in *N*-methyl-2-pyrrolidone (NMP) solvent. The resultant mixture was finely grained to prepare the slurry. The slurry was coated on the nickel foil using doctor blade method and dried in hot air oven for 24 h at 80 °C. The weight of the active materials was approximately 4 mg. The platinum foil, saturated calomel electrode (SCE) and active material coated nickel foil were used as counter, reference and working electrodes, respectively.

Characterization

The structural, morphological, elemental composition and the corresponding valance states of the prepared rGO/SnO_2 nanocomposites were characterized by the Bruker X-ray diffractometer (Model no. D8 Advance), HRSEM (Model no. Hitachi S4800), High-Resolution TEM (JEOL JEM-2000) and the Multi-technique X-ray Photoelectron Spectroscopy system Kratos AXIS ULTRA, respectively. The particle size of the SnO_2 nanoparticles was measured by dynamic light scattering technique using nano Partica nano particle analyzer (SZ-100), HORIBA scientific. The sensing response of the prepared pure and composite films were investigated before and after ozone exposure as follows; the functional groups interaction of the material with the ozone molecules were examined by the Versatile FT-IR Laboratory Spectrometer (Model no. ABB MB3000) in the region of 400–4000 cm^{-1}. The Raman spectra were recorded by the Horiba Jobin Yvon LabRAM HR micro Raman system with an excitation wavelength of 632 nm. The topographical variations of the sensing films were examined by Atomic force microscopy (Model no. MFP-3D Infinity AFM) for analyzing the surface properties of the films before and after ozone exposure. The ozone generator working on the basis of corona discharge method was used as an ozone source and the ppm of the ozone output was controlled by special dialing knob attached with the ozone generator. The electrochemical properties of the prepared materials were analyzed through cyclic voltammetry (CV), galvanostatic charge/discharge (GCD) and electrochemical impedance spectroscopic (EIS) analysis using Biologic Instrument (Model SP-150).

Results and discussion

Structural, morphological and compositional studies of SnO_2 and rGO/SnO_2 nanocomposite

Fig. 1 shows the X-Ray Diffraction (XRD) patterns of rGO, SnO_2 and rGO/SnO_2 nanocomposites. The XRD pattern of rGO exhibits two prominent peaks at the diffraction angles of 24.42° and 42.21° corresponding to (002) and (100) planes, respectively[59] and it is well-matched with the JCPDS no. 75-1621. Broad peaks are observed in the XRD pattern of SnO_2 at 26.57°, 33.73°, 51.81°and 64.73° corresponding to (110), (101), (211) and (112) planes, respectively,[34] which is matched with the JCPDS no. 01-072-1147. The broad diffraction peaks represent SnO_2 nanocrystalline particles. Further, the XRD pattern of rGO/SnO_2 nanocomposite shows rGO related peaks at 24.39° (002), 42.74° (110) and peaks related to SnO_2 at 26.53° (110), 33.69° (101), 51.84° (211) and 64.70° (112). These results confirm the

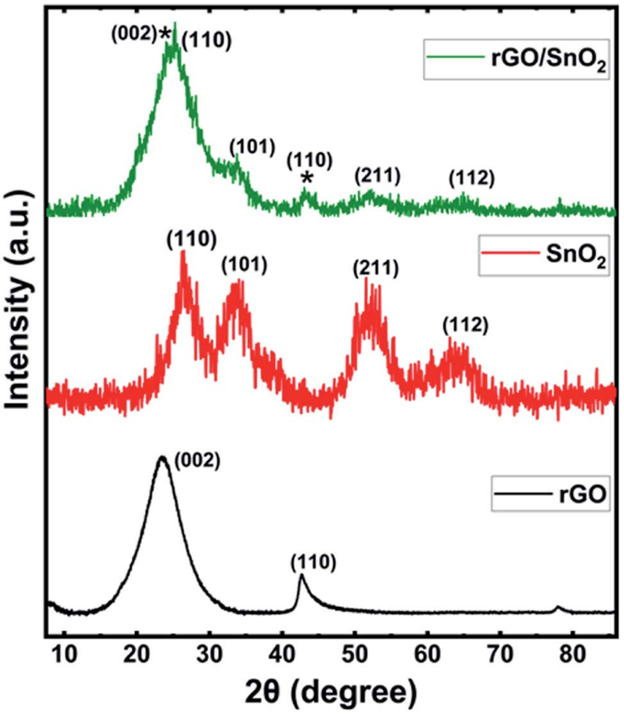

Fig. 1 X-ray diffraction patterns of rGO, SnO_2 and rGO/SnO_2 nanocomposite.

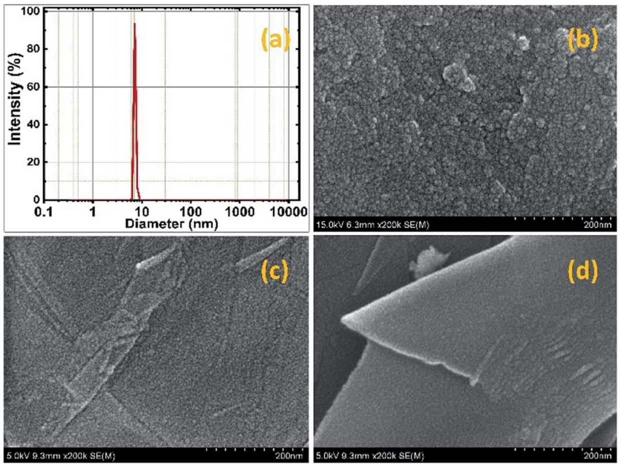

Fig. 2 DLS particle size analysis curve of SnO_2 nanoparticles (a), HR-SEM images of SnO_2 (b) and rGO/SnO_2 nanocomposite (c and d) in different area.

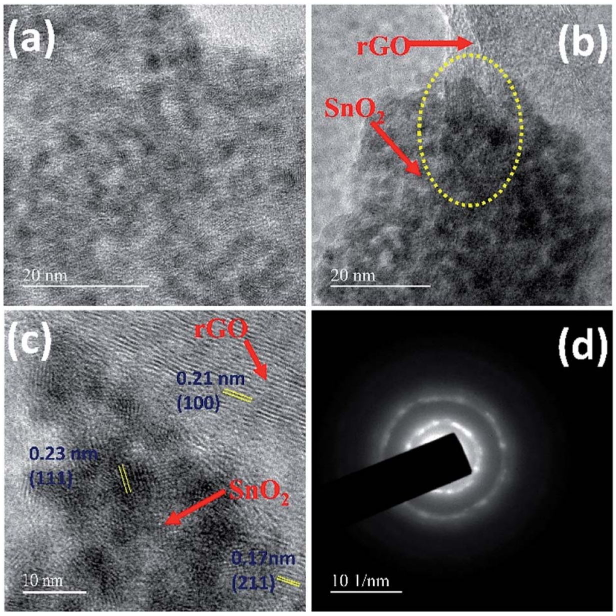

Fig. 3 HR-TEM images of SnO_2 (a), rGO/SnO_2 nanocomposite (b and c) and SAED pattern of rGO/SnO_2 nanocomposite (d).

formation of rGO/SnO_2 nanocomposite by the ultrasonic assisted solution process.

The mean particle size of the pure SnO_2 was measured as 7 nm by dynamic light scattering (DLS) as shown in Fig. 2a. The distribution of particles is more uniform with a narrow range of size variation from 6 to 9 nm. The morphological image of the SnO_2 is shown in Fig. 2b. It is significant to note that the ultra-small SnO_2 nanoparticles are formed in the present synthesis method. It may be explained as follows; during the synthesis process, the polyvinyl alcohol act as template, which can inhibit the nanoparticle overgrowth and agglomeration. Conversely, the capping agent, diethyl amine effectively passivated the surface and thereby controlled the particle size, which resulted in the formation of ultra-small nanoparticles.

Further, the morphological observations of rGO/SnO_2 nanocomposite are shown in Fig. 2c and d. It is obvious that the ultra-small SnO_2 nanoparticles are uniformly distributed on the rGO nanosheets. The SnO_2 nanoparticles act as an inter-sheet spacer, which inhibits restacking and collapsing between the rGO nanosheets. Besides, it is expected that the ultra-small SnO_2 nanoparticles provide high specific surface area and more active sites on the surface of the rGO/SnO_2 nanocomposites. Further, investigation was carried out through the HR-TEM analysis and the obtained images of pure SnO_2 and rGO/SnO_2 nanocomposite are shown in Fig. 3.

The uniformly grown ultra-small SnO_2 particles could be seen from the magnified image shown in Fig. 3a. In the case of rGO/SnO_2 nanocomposite (Fig. 3b and c), the ultra-small nanoparticles are found to be evenly embedded on the surface as well as at the interlayer spacing of rGO nanosheets as it is highlighted in dotted circle in Fig. 3b. The lattice fringes of rGO/SnO_2 nanocomposites are clearly visible in Fig. 3c. The measured *d*-spacing values of 0.23 nm (111), 0.17 nm (211) correspond to inter planar spacing of SnO_2 and 0.21 nm (100) is for rGO, which are well-matched with the observed XRD pattern of rGO/SnO_2 nanocomposite. Additionally, the SAED pattern of the rGO/SnO_2 nanocomposite, as shown in Fig. 3d, exhibits the ring pattern due to the presence of rGO and bright spots corresponding to SnO_2 nanoparticles. These studies confirm the formation SnO_2/rGO composite structure.

The energy dispersive X-ray (EDX) analysis of SnO_2 and rGO/SnO_2 nanocomposites confirm the material formation as shown in Fig. 4. The observed EDX spectrum of SnO_2 (Fig. 4a)

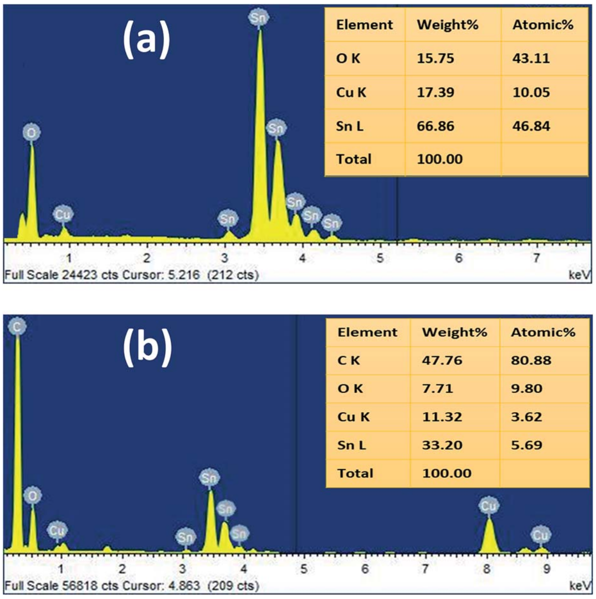

Element	Weight%	Atomic%
O K	15.75	43.11
Cu K	17.39	10.05
Sn L	66.86	46.84
Total	100.00	

Element	Weight%	Atomic%
C K	47.76	80.88
O K	7.71	9.80
Cu K	11.32	3.62
Sn L	33.20	5.69
Total	100.00	

Fig. 4 EDX spectra of SnO_2 (a) and rGO/SnO_2 nanocomposite (b).

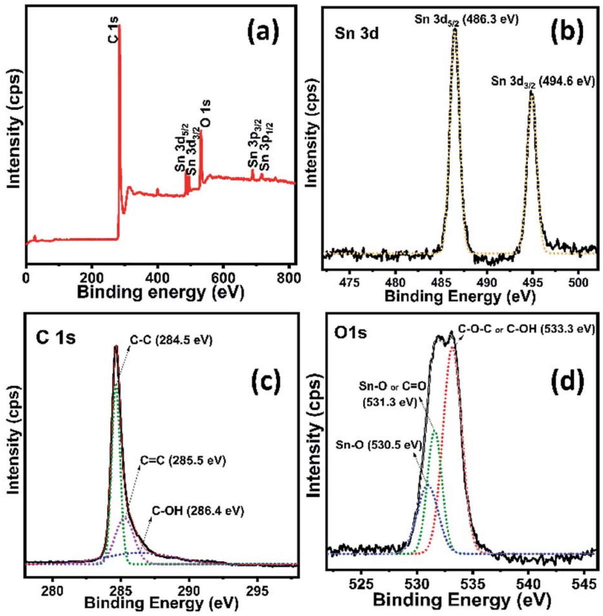

Fig. 5 XPS survey spectra of rGO/SnO_2 nanocomposite (a) and high-resolution spectra of Sn 3d (b), C 1s (c) and O 1s (d).

demonstrates the presence of Sn, O and Cu. Conversely, in the EDX spectrum of rGO/SnO_2 (Fig. 4b), carbon (C) peak additionally appears owing to the hybridisation of rGO into the SnO_2. The Cu peak is observed due to the copper substrate, which is used to hold the samples.

Fig. 5a shows the survey spectrum of rGO/SnO_2 nanocomposite, which confirms the nanocomposite formation. In Fig. 5b–d, all the core level high resolution spectra of elements are seen with fitting and deconvolution using Gaussian distribution. The core level spectrum of Sn 3d region of SnO_2 shows two characteristic peaks at 486.3 eV and 494.6 eV corresponding to Sn $3d_{5/2}$ and Sn $3d_{3/2}$, respectively as shown in Fig. 5b.[35] Fig. 5c demonstrates that the C 1s spectrum of rGO with high intense peak at 284.5 eV assigned to the graphite (sp^2) C–C bond and relatively very low intense shoulder peaks are observed at 285.5 eV (C═C) and 286.4 eV (C–OH), respectively.[36–38]

Further, the deconvoluted spectrum of O 1s (Fig. 5d) shows a most intensive peak at 533.3 eV assigned to the C–OH and/or C–O–C[39] and relatively two low intense peaks are noticed, owing to the binding energies of Sn–O (530.5 eV)[40] and C═O (531.3 eV).[39,40] Consequently, these peaks appear due to the interaction between the functional groups of rGO and SnO_2, that confirms the formation of rGO/SnO_2 nanocomposite. After the successful confirmation of the composite formation the prepared rGO/SnO_2 nanocomposite material was further investigated for the feasibility of ozone gas sensing and energy storage performances.

Investigations of the fabricated SnO_2 and rGO/SnO_2 films under ozone atmosphere

Functional investigations. Various functional groups of PVA, rGO and SnO_2 were identified in the FTIR analysis and the recorded spectra are shown in Fig. 6. The –OH stretching vibration was observed at 3452 cm^{-1} due to the PVA or physically absorbed water molecule on the surface of the film during the fabrication process. A strong peak at 1738 cm^{-1} and low intense peak at 1229 cm^{-1} correspond to –COOH groups.[23] Further, a peak at 1364 cm^{-1} corresponds to the C–C stretching vibration of PVA[41] and the Sn–O vibration of SnO_2 nanoparticles is observed in the region 520–562 cm^{-1}.[42–45] As shown in Fig. 6, the films of SnO_2 (Fig. 6a) and rGO/SnO_2 (Fig. 6c) have the oxygen and other functional groups before the ozone exposure and these peaks were disappeared after the exposure of ozone gas, which causes the changes in the morphological and other material characteristics of the films.

The Raman spectra of SnO_2 film before and after ozone exposure are shown in Fig. 7a. As can be seen from the Fig. 7a, three characteristic vibrational modes of SnO_2 at 473 cm^{-1} (E_g), 643 cm^{-1} (A_{1g}) and 786 cm^{-1} (B_{2g})[46] are observed. The PVA peaks observed around 880 cm^{-1}, 982 cm^{-1} and 1173 cm^{-1} correspond to the fan or twist modes in cyndio or isotactic sequences.[47] After exposing the ozone gas on the surface of the film, SnO_2 related peaks are clearly visible, in particular, the intensity of the peak at 786 cm^{-1} (B_{2g}) is found to increase, which contributes that the ozone interacts on the SnO_2 film surface. Conversely, in the rGO/SnO_2 nanocomposite film, the SnO_2 related peaks appear at 490 cm^{-1}, 647 cm^{-1} and 786 cm^{-1} (B_{2g}), due to the introduction of PVA and rGO (Fig. 7b). Further, SnO_2 related peaks are shifted to higher frequency region, which supports the rGO/SnO_2 nanocomposite formation. The PVA peaks at 818 cm^{-1} and 914 cm^{-1} correspond to the fan or twist modes in cyndio or isotactic sequences.[47] The peaks at 1098 cm^{-1} and 1230 cm^{-1} are attributed to the O–H deformation and C–O valance bond vibrational modes of secondary alcohols in the PVA matrix.[47]

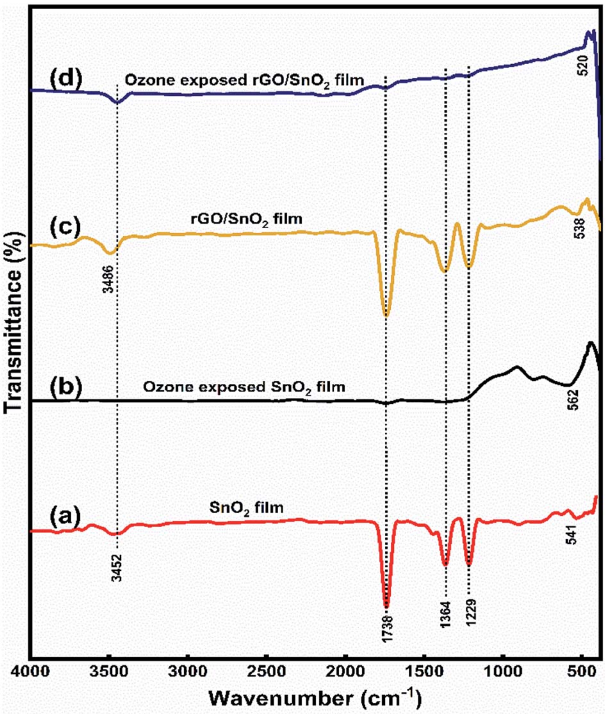

Fig. 6 FTIR spectra of SnO_2 film (a), ozone exposed SnO_2 (b), rGO/SnO_2 film (c) and ozone exposed rGO/SnO_2 film (d).

In Fig. 7b, the D and G bands are observed at 1330 cm^{-1} and 1574 cm^{-1}, respectively. The G band corresponds to E_{2g} phonon

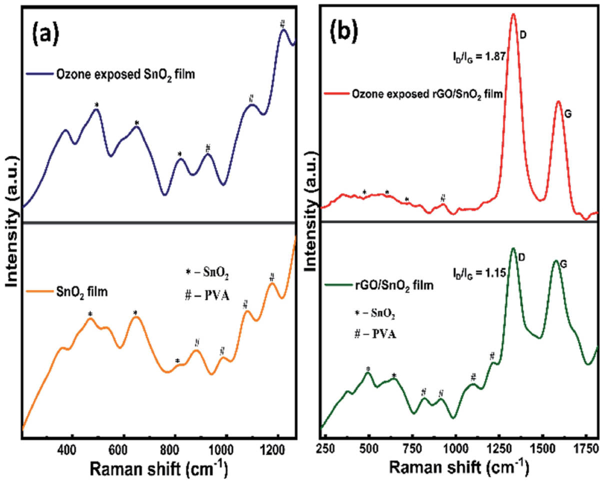

Fig. 7 Raman spectra of SnO_2 & ozone exposed SnO_2 film (a) and rGO/SnO_2 & ozone exposed rGO/SnO_2 film (b).

vibrations of sp^2 hybridized carbon atoms in the isolated double bonds of graphene lattice and the D band analogous to the *K*-point phonons' one-phonon defect-assisted process of vibrations with A_{1g} symmetry.[48] Therefore, the I_D/I_G ratio provides the structural imperfections in the rGO, owing to the attachment of functional groups on the plane of rGO.[48] The I_D/I_G ratio of the rGO/SnO_2 nanocomposite film is calculated as 1.15, which strongly supports the attachment of the SnO_2 nanoparticles on the surface and interlayers of rGO as seen in the morphological studies (HRSEM and HRTEM).

After passing the ozone gas, the intensity of the D and G bands is found to increase and the bands are noticed at 1331 cm^{-1} and 1590 cm^{-1}, respectively (Fig. 7b). Most of the PVA peaks disappear and the SnO_2 related peak intensities decreased owing to the interaction of the ozone molecules. The I_D/I_G ratio of the ozone exposed rGO/SnO_2 film is calculated as 1.87, which explains the enrichment of graphene content after the ozone interaction.

Surface variations. The surface topographical variations of SnO_2 and rGO/SnO_2 nanocomposites have been analysed before and after ozone exposure as shown in the Fig. 8. The surface topography of the fabricated SnO_2 film (Fig. 8a) reveals that the rough surface of the film is found to be relatively higher before ozone exposure and it is relatively decreased in the ozone exposed SnO_2 film (Fig. 8b). The SnO_2 nanoparticles decorated rGO sheets are observed in the rGO/SnO_2 nanocomposite film as shown in the Fig. 8c. After exposing the ozone gas on the surface of the rGO/SnO_2 nanocomposite film, the flattened morphology is observed (Fig. 8d), which clearly illustrates the development of the graphene rich layer after exposing the ozone gas, which agrees with the Raman and FTIR results.

The surface roughness profiles of SnO_2, ozone exposed SnO_2 film, rGO/SnO_2 film and ozone exposed rGO/SnO_2 film have been analysed for studying the morphological variations. Fig. 9a shows the variation of surface roughness of SnO_2 film and it varied from −2 to 2 nm, which is found to be decreased to −1.3 to 1 nm, after exposing the ozone gas on the surface of the SnO_2 film (Fig. 9b). The variations of surface roughness of rGO/SnO_2 nanocomposite are in the range of −4 to 4 nm as shown in Fig. 9c and it is found to decrease after exposure of ozone, which may be due to the removal of rGO, PVA functional groups from the surface of the rGO/SnO_2 film (Fig. 9d). Therefore, the ozone exposure induces morphological variations based on the ozone environment that leads to the electrical variation in the sensing film.

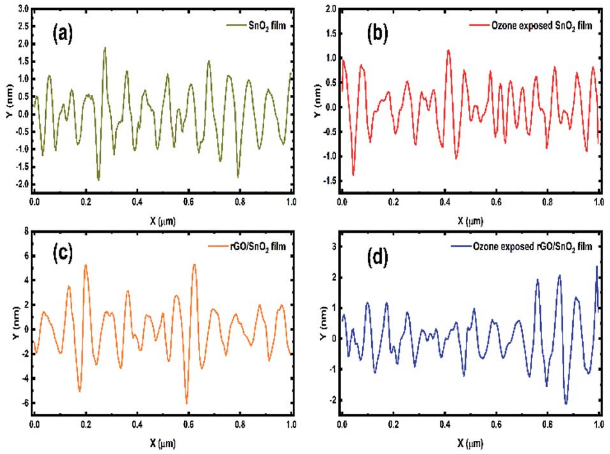

Fig. 9 Surface roughness profiles of SnO_2 (a) ozone exposed SnO_2 film (b), rGO/SnO_2 nanocomposite (c) and ozone exposed rGO/SnO_2 nanocomposite film (d).

Electrical properties. The variation in the electrical properties of SnO_2 and rGO/SnO_2 coated films were studied at room temperature by applying the potential through the Keithley voltage–current (*V–I*) measurement system as a function of ozone exposure levels ranging from 0.1 ppm to 1.0 ppm and the observed results are shown in Fig. 10. The initial resistance of each film measured in air atmosphere before introducing the

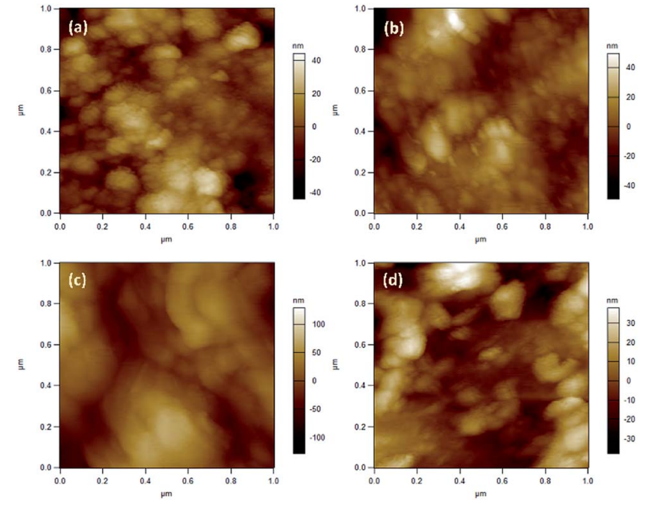

Fig. 8 AFM images of SnO_2 (a) ozone exposed SnO_2 film (b), rGO/SnO_2 nanocomposite (c) and ozone exposed rGO/SnO_2 nanocomposite film (d).

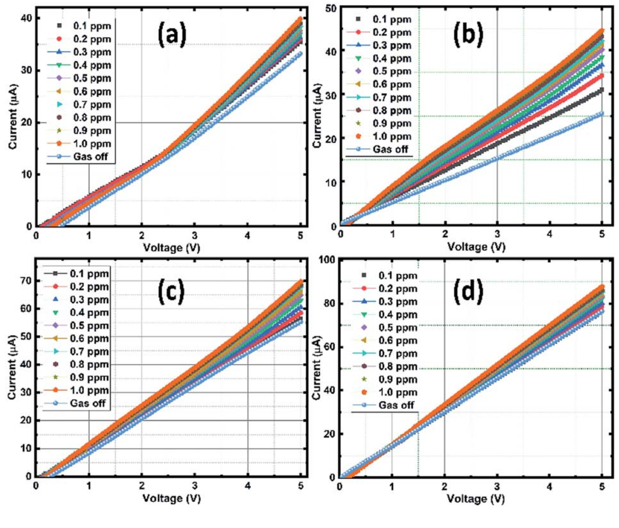

Fig. 10 *V–I* measurements of the sensing films at different ozone concentration: SnO_2 (a), rGO/SnO_2-S1 (b), rGO/SnO_2-S2 (c) and rGO/SnO_2-S3 (d).

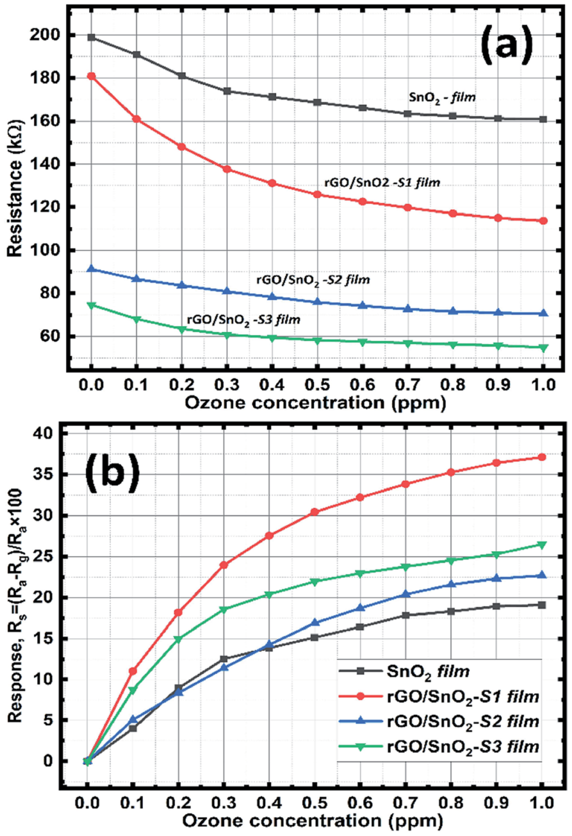

Fig. 11 Resistance variation (a) and the ozone sensing response curves of the SnO_2 & rGO/SnO_2 nanocomposite films as a function of ozone concentration (b).

ozone gas and the measured data is shown in *V–I* plot as "gas off". After that, the *V–I* measurement was taken by exposing the ozone gas at various concentrations onto the SnO_2 and rGO/SnO_2 films.

In Fig. 10a, the pure SnO_2 film exhibits a gradual current increment, while increasing the ozone concentration from 0.1 to 1 ppm. It is observed that the *V–I* characteristic lines start to bunch at a threshold voltage that ranges approximately between 2 to 3 V and then increases with respect to the higher applied potential and ozone concentrations. The observed increase in conductivity beyond the threshold voltage regime (2–3 V) promises the optimum sensing performance of the SnO_2 film. Whereas, in the case of composite films of rGO/SnO_2-S1, rGO/SnO_2-S2 & rGO/SnO_2-S3, the current rate is varied with the concentration of ozone in the voltage range of approximately 0.5–1.5 V as shown in the Fig. 10b and c.

The higher electrical response is achieved for the rGO/SnO_2-S2 and rGO/SnO_2-S3 films, due to the presence of rGO. However, the rGO/SnO_2-S1 show a quantifiable current variation with respect to the ozone concentration at 1 V that suggest the best sensing performance and lower operating voltage of the rGO/SnO_2-S1 film. Hence, based on the *V–I* data, the electrical resistance of the ozone exposed sensing films was calculated, and the results were plotted as a function of ozone concentration (Fig. 11a). Further investigations revealed that the rGO/SnO_2 nanocomposite films exhibit relatively high response towards the ozone concentrations compared to pure SnO_2. As can be seen from the Fig. 11b, the composite films show the maximum ozone response (20–38%) at 1.0 ppm compared to the SnO_2 film (18%). However, it must be noted that the rGO/SnO_2-S1 with 3 μm thickness shows the proportional response to the entire range (0.1–1 ppm) of exposed ozone concentrations.

Sensing mechanism. The sensing mechanism of the SnO_2 and rGO/SnO_2 films involve the splitting of O_3 molecule into O_2 and adsorptive oxygen ions (O^{-ads}) by reacting with excess electrons of SnO_2. The O^{-ads} react with the functional groups of pure and composite films, which effectively removed the residual functional groups of rGO and PVA matrix as evidenced by the FTIR and Raman analyses (Fig. 6 and 7). The AFM analysis support the mechanism that the surface roughness was reduced in the ozone exposed pure and nanocomposite films as seen in the Fig. 8 and 9. Moreover, large I_D/I_G ratio of the ozone exposed rGO/SnO_2 film (Fig. 7b) confirms that the ozone exposure enhances the sp^2 network in the rGO layer, which favors the increased electrical conductivity during ozone exposure. Moreover, rGO/SnO_2 composite exhibit higher electrical conductivity due to the presence of ultra-small SnO_2 particles on the surface and at the interlayer of rGO nanosheets as depicted

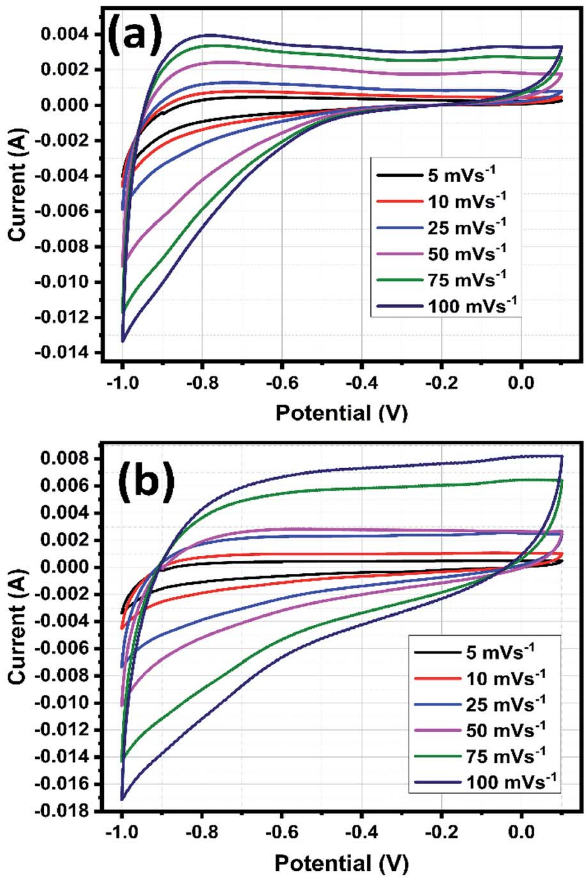

Fig. 12 Cyclic voltammetric curves of SnO_2 (a) and rGO/SnO_2 nanocomposite (b).

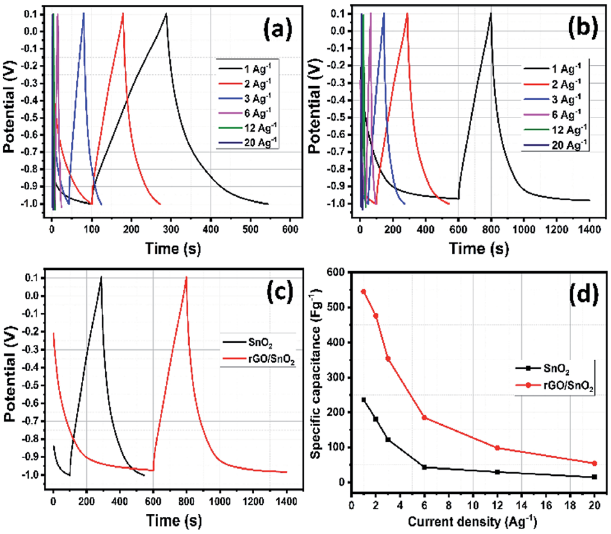

Fig. 13 GCD studies of SnO_2 (a) and rGO/SnO_2 nanocomposite (b) at different current densities, GCD study of SnO_2 & rGO/SnO_2 nanocomposite at the current density of 1 A g^{-1} (c) and specific capacitance *versus* current density (d).

in the Fig. 2c, d, 3b and c which enhanced the ozone sensing performance.

Electrochemical performance of the rGO/SnO_2 nanocomposite

The CV analysis were carried out by varying the scan rates from 5 to 100 mV s^{-1} within the potential range from −1.0 to 0.1 V in 1 M of H_2SO_4 electrolyte solution.[49] The recorded CV curves are shown in Fig. 12a and b, the shape of the curves explains the capacitive behaviour of the electrode materials and the CV curves doesn't show any redox peaks but all curves exhibited roughly in rectangular shape, which signifying the formation of electric double layer capacitor (EDLC) charge storage mechanism.[24] The CV curves remain stable and no distortion occurred when increasing scan rate up to 100 mV s^{-1} for both SnO_2 and rGO/SnO_2 electrodes representing high stability and quick interfacial charge transfer of the electrode materials.[50] The current peak increased gradually with an increase of scan rate from 5 to 100 mV s^{-1}, which is attributed to the superior electrochemical features of SnO_2 and rGO/SnO_2 electrodes.[25]

Also, the larger voltage window 1.1 V indicates the high energy density of SnO_2 and rGO/SnO_2 electrode materials. It is well known that an integral area of the CV curves is directly proportional to the specific capacitive behaviour of the electrodes. In the present study, rGO/SnO_2 electrode material exhibited higher integral area than that of pure SnO_2, which implies the superior specific capacitance feature of the rGO/SnO_2 electrode material.

The electrochemical properties of the electrode materials were further evaluated by galvanostatic charge/discharge (GCD) analyses as shown in Fig. 13a and b. The linear profile of GCD curves confirms the EDLC behavior which is more consistent with the CV results.[51] When compared with the SnO_2 electrode, the rGO/SnO_2 provides long discharge time confirming the superior specific capacitive nature. At lower current densities, the charge/discharge process took longer time which is ascribed to the adequate interaction of electrolyte ions during charging discharging process as shown in Fig. 13c. The specific capacitance (C_{sp}) of the electrode can be calculated using eq.,[52]

$$C_{sp} = I\Delta t/m\Delta V$$

where ΔV denotes fixed potential window (V), m mass of the active material (mg) in the electrodes, I discharge current density (A) and Δt is the discharge time (s). The discharge curve of the SnO_2 and rGO/SnO_2 electrodes provides the 236 and 545 F g^{-1} of the specific capacitance at a current density of 1 A g^{-1}. The specific capacitance of the rGO/SnO_2 electrode is 2-fold increases when compared with pure SnO_2 electrode material. Also, the 545 F g^{-1} of specific capacitance obtained by rGO/SnO_2 is higher than previous reported literature based on SnO_2 and rGO/SnO_2 materials as shown in Table 1.

The higher specific capacitance of rGO/SnO_2 composite electrode is due to the following reason: (i) the homogeneous distribution of ultrasmall SnO_2 materials on rGO sheets in the course of influence of synergistic effect, which is more encouraging for electrochemical process and thus, ensuing high specific capacitance (ii) the ultra-small SnO_2 materials provide more active sites for electrochemical progression and reduced the electrolyte ion transport pathways. (iii) Thin rGO

Table 1 Comparison of the specific capacitance of rGO/SnO_2 electrode material with reported data of similar kind of material

Material	Electrolyte	Specific capacitance (F g^{-1})	Current density (A g^{-1})	Ref.
rGO/SnO_2	1 M KOH	35	0.1	53
Graphene–SnO_2	1 M Na_2SO_4	158	0.1	54
SnO_2/GNS	1 M Na_2SO_4	184.6	0.1	55
SnO_2/rGO@NF	PVA/KOH	229.1	1	56
SnO_2QDs/rGO	1 M Na_2SO_4	253.3	1	57
SnO_2/rGO	1 M Na_2SO_4	262.2	0.1	28
SnO_2/rGO	2 M KOH	310	2	29
SnO_2/rGO	1 M H_2SO_4	337.52	0.5	49
SnO_2/graphene	1 M Na_2SO_4	364.3	1	24
SnO_2@NGO	6 M KOH	378	4	26
rGO/SnO_2	1 M H_2SO_4	545	1	This work

nanosheets exhibit attractive features such as high electrical conductivity, high surface area, and high flexibility which may help to enhance the specific capacitance of the composite materials.

Rate capability is one of the important parameters for supercapacitor electrode materials. For evaluation of rate capability of SnO_2 and rGO/SnO_2 electrodes, the GCD studies were carried out with various current densities as shown in Fig. 13d. It is perfectly visible that the specific capacitance slightly decreases with increasing of current density due to time limitation process. At low current density, the electrolyte ions experience larger time to meet the electrode materials, which enhance the electrode materials utilization and thus increases the specific capacitance. On the other hand, the outer surface electrode materials only utilized by electrolyte ions due to shorter time at higher current densities which decreases the specific capacitance.[27]

Long term cycling stability is a significant factor for evaluating the electrode materials for supercapacitor applications. Cycling stability analyses were carried out for both SnO_2 and rGO/SnO_2 electrodes at 20 A g^{-1} current density for continuous 5000 charge discharge cycles as shown in Fig. 14. Fascinatingly, the specific capacitance slightly increases to 102% at 1400th cycles in rGO/SnO_2 electrode, which signifies the activation process of electrode materials.[58]

In the endeavour, the accumulation of electrolyte ions contributes to the activation of electrode materials which is advantageous to stimulate the internal active region and enhancing the specific capacitance. After that, the specific capacitance gradually decreases and attains 89 and 96% for SnO_2 and rGO/SnO_2 electrodes, respectively. When compared with SnO_2, the rGO/SnO_2 electrode exhibiting good cyclic stability features. This phenomenon is due to the fact that the SnO_2 material may act as a spacer material between the two-neighbourhood reduced graphene oxide nanosheets and thus it helps to reduce the restacking of rGO nanosheets which always maintain the high surface area during cyclic stability analysis.[59] Furthermore, this factor enhances the surface area utilization feature of electrolyte ions and thus it keeps specific capacitance maximum for 5000 cycles. In addition, the aforementioned key advantage of rGO/SnO_2 electrode is attributed to excellent contact between SnO_2 and rGO nanosheets. Hence, rGO/SnO_2 is a significant electrode material for future supercapacitor device application.

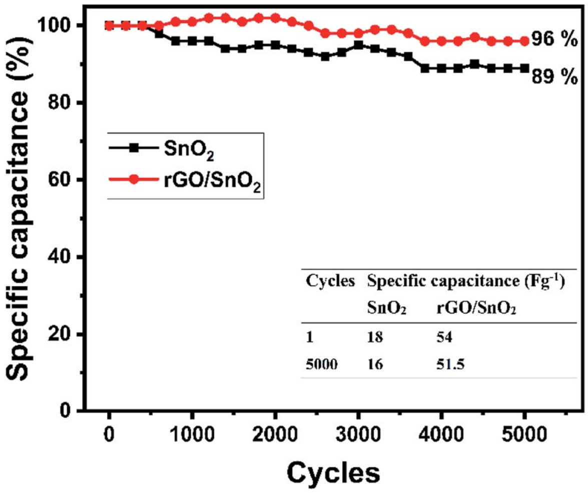

Cycles	Specific capacitance (Fg^{-1})	
	SnO_2	rGO/SnO_2
1	18	54
5000	16	51.5

Fig. 14 Cyclic stability of SnO_2 and rGO/SnO_2 nanocomposite electrode at 20 A g^{-1} for 5000 charge/discharge cycles.

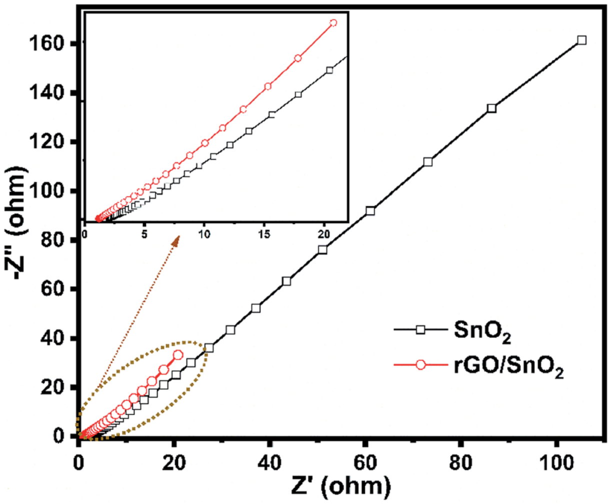

Fig. 15 Electrochemical impedance spectra of SnO_2 and rGO/SnO_2 nanocomposite.

The electrochemical impedance spectra were recorded for the prepared electrode materials of SnO_2 and rGO/SnO_2 nanocomposite as shown in Fig. 15. Both the spectra exhibited a depressed semicircle in the high frequency region followed by a linear region appeared in the low frequency range. The depressed semicircle explains the interfacial charge transfer process at the electrode/electrolyte interface and the linear region describes about the Warburg impedance owing to the diffusion dominant charge transport in the electrolyte and surface of the electrode materials.[60]

During the charging process the charges carried by the ions may diffuse towards the electrode material and thereby

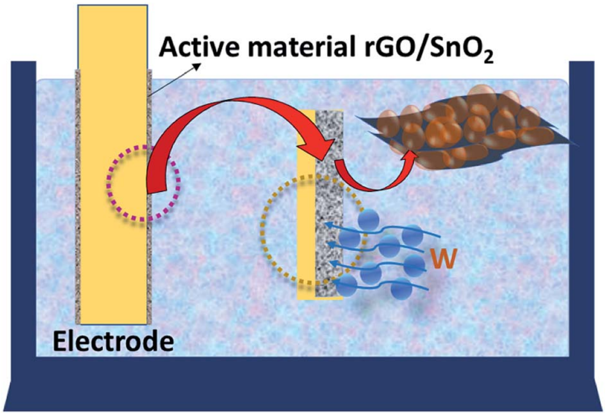

Fig. 16 Schematic representation of the charge storage mechanism of rGO/SnO_2 nanocomposite.

produces the electric double-layer capacitance (EDLC) as shown schematically in Fig. 16. Further, the intercalation of ultra-small SnO_2 between the stacks of rGO nanosheets favors a highly porous nature (Fig. 16) and fast charge transfer process thus leads to the high charge storage capacity of the rGO/SnO_2 electrode material than that of pure SnO_2 nanoparticles.

Conclusions

Ultra-small SnO_2 nanoparticles synthesised by hydrothermal route were composited with chemically synthesised rGO nanosheets. The morphological analyses show a uniform distribution of SnO_2 nanoparticles on the surface and at the interlayer spacing of the rGO nanosheets. The XRD, FTIR and Raman analyses confirmed the formation of pure ultra-small SnO_2 and rGO/SnO_2 nanocomposite. XPS studies strongly support the rGO/SnO_2 nanocomposite formation during ultrasonication process. Structural, functional, morphological and electrical conductivity studies reveal that the fabricated SnO_2 and rGO/SnO_2 nanocomposite films have a good interaction with the ozone gas. Among the fabricated composite films. The rGO/SnO_2-S1 film exhibits high ozone sensing response (38%) at room temperature. Additionally, the electrochemical performance of SnO_2 and rGO/SnO_2 nanocomposites exhibited higher specific capacitance value (545 F g^{-1}) at 1 A g^{-1} and higher cyclic stability of 96% at 20 A g^{-1} for continuous 5000 charge–discharge cycles than the pure SnO_2. The synthesised rGO/SnO_2 nanocomposite material showed best ozone sensing and energy storage performance than the pure SnO_2 nanoparticles.

Conflicts of interest

There are no conflicts to declare.

Acknowledgements

This work was financially supported by University Grants Commission (UGC) sponsored Rajiv Gandhi National Fellowship for Students with Disabilities (RGNFD), New Delhi. We acknowledge the facilities extended by the University of Madras DST PURSE research facility for DLS and AFM analysis.

Notes and references

1 A. Barone, M. Otero-Losada, A. M. Grangeat, G. Cao, F. Azzato, A. Rodriguez and J. Milei, *Int. J. Cardiol.*, 2016, **223**, 258–261.

2 J. Xue, Y. Zhang, Y. Liu and M. Gamal El-Din, *Water Res.*, 2016, **105**, 444–455.

3 L. Bilińska, M. Gmurek and S. Ledakowicz, *Process Saf. Environ. Prot.*, 2017, **109**, 420–428.

4 R. G. Rice, *Commercial applications of ozone in food processing*, Woodhead Publishing Ltd, 2010, vol. 3.

5 M. F. Kamaroddin, J. Hanotu, D. J. Gilmour and W. B. Zimmerman, *Algal Res.*, 2016, **17**, 217–226.

6 D. Nuvolone, D. Petri and F. Voller, *Environ. Sci. Pollut. Res.*, 2018, **25**, 8074–8088.

7 J. E. Goodman, R. L. Prueitt, J. Chandalia and S. N. Sax, *J. Appl. Toxicol.*, 2014, **34**, 516–524.

8 X. He, J. E. Yoo, M. H. Lee and J. Bae, *Nanotechnology*, 2017, **28**, 245402.

9 S. N. Pusawale, P. R. Deshmukh and C. D. Lokhande, *Appl. Surf. Sci.*, 2011, **257**, 9498–9502.

10 D. Ganguly, D. Pahari, N. S. Das, P. Howli, B. Das, D. Banerjee and K. K. Chattopadhyay, *J. Electroanal. Chem.*, 2016, **778**, 12–22.

11 S. Liu, J. Wu, J. Zhou, G. Fang and S. Liang, *Electrochim. Acta*, 2015, **176**, 1–9.

12 M. Saranya, R. Ramachandran and F. Wang, *J. Sci. Adv. Mater. Devices*, 2016, **1**, 454–460.

13 M. Tonezzer, J. H. Kim, J. H. Lee, S. Iannotta and S. S. Kim, *Sens. Actuators, B*, 2019, **281**, 670–678.

14 M. Hijazi, M. Rieu, V. Stambouli, G. Tournier, J. P. Viricelle and C. Pijolat, *Sens. Actuators, B*, 2018, **256**, 440–447.

15 G. Korotcenkov, V. Brinzari and B. K. Cho, *Sens. Actuators, B*, 2017, **243**, 507–515.

16 S. Mills, M. Lim, B. Lee and V. Misra, *ECS J. Solid State Sci. Technol.*, 2015, **4**, S3059–S3061.

17 M. Belaqziz, M. Amjoud, A. Gaddari, B. Rhouta and D. Mezzane, *Superlattices Microstruct.*, 2014, **71**, 185–189.

18 J. Du, S. He, R. Zhao, S. Chen, T. Guo and H. Wang, *Mater. Lett.*, 2017, **186**, 318–321.

19 S. Mohammad-Yousefi, S. Rahbarpour and H. Ghafoorifard, *Mater. Chem. Phys.*, 2019, **227**, 148–156.

20 G. Korotcenkov, V. Brinzari, L. B. Gulina and B. K. Cho, *Appl. Surf. Sci.*, 2015, **353**, 793–803.

21 Y. Fukai, Y. Kondo, S. Mori and E. Suzuki, *Electrochem. Commun.*, 2007, **9**, 1439–1443.

22 F. Chen and M. Liu, *Chem. Commun.*, 1999, 1829–1830.

23 N. Hu, Z. Yang, Y. Wang, Z. Liling, Y. Wang, X. Huang, H. Wei, L. Wei and Y. Zhang, *Nanotechnology*, 2013, **25**, 025502.

24 S. P. Lim, N. M. Huang and H. N. Lim, *Ceram. Int.*, 2013, **39**, 6647–6655.

25 H. Zhang, A. Xie, C. Wang, H. Wang, Y. Shen and X. Tian, *ChemPhysChem*, 2014, **15**, 366–373.

26 S. Ramesh, H. M. Yadav, Y. J. Lee, G. W. Hong, A. Kathalingam, A. Sivasamy, H. S. Kim, H. S. Kim and J. H. Kim, *Sci. Rep.*, 2019, **9**, 1–10.

27 T. Liu, H. Chai, D. Jia, Y. Su, T. Wang and W. Zhou, *Electrochim. Acta*, 2015, **180**, 998–1006.

28 Y. Zhang, M. Liu, S. Sun and L. Yang, *Adv. Compos. Lett.*, 2020, **29**, 2633366X2090983.

29 M. Chen, H. Wang, L. Li, Z. Zhang, C. Wang, Y. Liu, W. Wang and J. Gao, *ACS Appl. Mater. Interfaces*, 2014, **6**, 14327–14337.

30 N. I. Kovtyukhova, P. J. Ollivier, B. R. Martin, T. E. Mallouk, S. A. Chizhik, E. V. Buzaneva and A. D. Gorchinskiy, *Chem. Mater.*, 1999, **11**, 771–778.

31 M. Shanmugam and R. Jayavel, *J. Nanosci. Nanotechnol.*, 2015, **15**, 7195–7201.

32 H. C. Hsu, I. Shown, H. Y. Wei, Y. C. Chang, H.-Y. Du, Y.-G. Lin, C.-A. Tseng, C.-H. Wang, L. C. Chen, Y.-C. Lin and K. H. Chen, *Nanoscale*, 2012, 262–268.

33 J. Jayachandiran, M. Arivanandhan, O. Padmaraj, R. Jayavel and D. Nedumaran, *Adv. Compos. Hybrid Mater.*, 2020, **3**, 16–30.

34 J. Du, R. Zhao, Y. Xie and J. Li, *Appl. Surf. Sci.*, 2015, **346**, 256–262.

35 A. Kar, S. Sain, D. Rossouw, B. R. Knappett, S. K. Pradhan and A. E. H. Wheatley, *Nanoscale*, 2016, **8**, 2727–2739.

36 C.-H. Chuang, Y.-F. Wang, Y.-C. Shao, Y.-C. Yeh, D.-Y. Wang, C.-W. Chen, J. W. Chiou, S. C. Ray, W. F. Pong, L. Zhang, J. F. Zhu and J. H. Guo, *Sci. Rep.*, 2014, **4**, 4525.

37 A. Ariharan, B. Viswanathan and V. Nandhakumar, *Graphene*, 2017, **06**, 41–60.

38 N. A. Kumar, H. Nolan, N. McEvoy, E. Rezvani, R. L. Doyle, M. E. G. Lyons and G. S. Duesberg, *J. Mater. Chem. A*, 2013, **1**, 4431–4435.

39 R. Tian, Y. Zhang, Z. Chen, H. Duan, B. Xu, Y. Guo, H. Kang, H. Li and H. Liu, *Sci. Rep.*, 2016, **6**, 19195.

40 J. Liang, C. Yuan, H. Li, K. Fan, Z. Wei, H. Sun and J. Ma, *Nano-Micro Lett.*, 2018, **10**, 21.

41 A. S. Roy, S. Gupta, S. Sindhu, A. Parveen and P. C. Ramamurthy, *Composites, Part B*, 2013, **47**, 314–319.

42 M. M. Rashad, A. A. Ismail, I. Osama, I. A. Ibrahim and A. H. T. Kandil, *Arabian J. Chem.*, 2014, **7**, 71–77.

43 S. Sagadevan and J. Podder, *Mater. Res.*, 2016, **19**, 420–425.

44 T. A. Dontsova, S. V. Nagirnyak, V. V. Zhorov and Y. V. Yasiievych, *Nanoscale Res. Lett.*, 2017, **12**, 332.

45 M. Shanmugam, A. Alsalme, A. Alghamdi and R. Jayavel, *Mater. Express*, 2015, **5**, 319–326.

46 V. Agrahari, M. C. Mathpal, M. Kumar and A. Agarwal, *J. Alloys Compd.*, 2015, **622**, 48–53.

47 I. Y. Prosanov and A. A. Matvienko, *Phys. Solid State*, 2010, **52**, 2203–2206.

48 S. Navazani, A. Shokuhfar, M. Hassanisadi, A. Di Carlo and N. Shahcheraghi, *Mater. Sci. Semicond. Process.*, 2018, **88**, 139–147.

49 P. J. Sephra, P. Baraneedharan, M. Sivakumar, T. D. Thangadurai and K. Nehru, *Mater. Res. Bull.*, 2018, **106**, 103–112.

50 K. H. Lee, Y. W. Lee, S. W. Lee, J. S. Ha, S. S. Lee and J. G. Son, *Sci. Rep.*, 2015, **5**, 1–10.

51 T. Y. Kim, H. W. Lee, M. Stoller, D. R. Dreyer, C. W. Bielawski, R. S. Ruoff and K. S. Suh, *ACS Nano*, 2011, **5**, 436–442.

52 X. Li, X. Li, G. Wang, X. Wang and J. Ji, *J. Mater. Chem. A*, 2013, **1**, 10103–10106.

53 A. Choudhari, B. A. Bhanvase, V. K. Saharan, P. H. Salame and Y. Hunge, *Ceram. Int.*, 2020, **46**, 11290–11296.

54 S. R. Eedulakanti, A. K. Gampala, K. Venkateswara Rao, C. Shilpa Chakra, V. Gedela and R. Boddula, *Mater. Sci. Energy Technol.*, 2019, **2**, 372–376.

55 M. Liu, S. Sun, L. Yang and S. Yin, *Int. J. Mater. Res.*, 2018, **109**, 743–750.

56 R. Hu, J. Zhao and J. Zheng, *Mater. Lett.*, 2017, **197**, 59–62.

57 R. Hu, J. Zhao and J. Zheng, *Int. J. Electrochem. Sci.*, 2020, **15**, 6257–6268.

58 J. Xiao and S. Yang, *J. Mater. Chem.*, 2012, **22**, 12253–12262.

59 X. Yang, J. Zhu, L. Qiu and D. Li, *Adv. Mater.*, 2011, **23**, 2833–2838.

60 H. T. Rahal, A. M. Abdel-Gaber and R. Awad, *Int. J. Electrochem. Sci.*, 2017, **12**, 10115–10128.